

---

---

## Redetermination of Galactic Spiral Density Wave Parameters Based on Spectral Analysis of Maser Radial Velocities

A.T. Bajkova<sup>1</sup> and V.V. Bobylev<sup>1,2</sup>

<sup>1</sup> *Pulkovo Astronomical Observatory, Russian Academy of Sciences*

<sup>2</sup> *Sobolev Astronomical Institute, St. Petersburg State University, Russia*

**Abstract**—To redetermine the Galactic spiral density wave parameters, we have performed a spectral (Fourier) analysis of the radial velocities for 44 masers with known trigonometric parallaxes, proper motions, and line-of-sight velocities. The masers are distributed in a wide range of Galactocentric distances ( $3.5 < R < 13.2$  kpc) and are characterized by a wide scatter of position angles  $\theta$  in the Galactic  $XY$  plane. This has required an accurate allowance for the dependence of the perturbation phase both on the logarithm of the Galactocentric distances and on the position angles of the objects. To increase the significance of the extraction of periodicities from data series with large gaps, we have proposed and implemented a spectrum reconstruction method based on a generalized maximum entropy method. As a result, we have extracted a periodicity describing a spiral density wave with the following parameters from the maser radial velocities: the perturbation amplitude  $f_R = 7.7_{-1.5}^{+1.7}$  km s<sup>-1</sup>, the perturbation wavelength  $\lambda = 2.2_{-0.1}^{+0.4}$  kpc, the pitch angle of the spiral density wave  $i = -5_{-0.9}^{+0.2}$ °, and the phase of the Sun in the spiral density wave  $\chi_{\odot} = -147_{-17}^{+3}$ °.

## 1 Introduction

A spectral analysis of the residual space velocities for various young Galactic objects (HI clouds, OB stars, open clusters younger than 50 Myr, masers) tracing the spiral arms was used, for example, by Clemens (1985), Bobylev et al. (2008), and Bobylev and Bajkova (2010). As a result, such spiral density wave parameters (in accordance with the model of Lin and Shu (1964)) as the pitch angle, the perturbation amplitude and wavelength, and the phase of the Sun in the spiral density wave were determined. The spectral analysis performed previously was the simplest periodogram analysis (based on the Fourier transform) of the residual space velocities for the objects as functions of their Galactocentric distances. In this case, the position angles of the objects in the Galactic  $XY$  plane were disregarded.

Obviously, the previously applied approach may be considered only as the first approximation that is accurate enough only when the objects being analyzed occupy a comparatively small range of Galactocentric distances. For example, in the case of OB stars and open clusters localized within  $\approx 2 - 3$  kpc of the Sun, this first approximation is quite adequate. In contrast, in the case of using the currently available data on masers distributed in a wide range of Galactocentric distances,  $3 < R < 14$  kpc, a more accurate processing that takes into account both the logarithmic dependence of the perturbation

phase on the Galactocentric distances and the dependence of the perturbation phase on the position angles of the objects is required. As will be shown below, our periodogram analysis allows the significance of the extraction of periodicities from measurements to be increased considerably.

Previously, we (Bobylev and Bajkova 2010) performed a spectral analysis of the space velocities for 28 masers. At present, highly accurate VLBI measurements are available already for 44 masers. This is of great interest in redetermining the spiral density wave parameters from objects of this class.

Thus, the goal of this paper is the development of a new, more accurate approach to a periodogram analysis of the residual velocities for Galactic objects and its application to redetermine the Galactic spiral density wave parameters from masers distributed in a wide range of Galactocentric distances. In addition, to increase the significance of the extraction of periodicities from data series with large gaps, we proposed and implemented a method of analysis based on the reconstruction of the spectra for nonuniform data series using a generalized maximum entropy method (Bajkova 1992).

The paper is structured as follows. In the first section, we consider the details of the developed periodicity extraction method and present the results of its testing on model data. The second section is devoted directly to an analysis of the radial velocities for the largest number of masers known to date for which highly accurate measurements of the trigonometric parallaxes, proper motions, and line-of-sight velocities are available.

## 2 THE METHOD

### 2.1 Basic Relations

The velocity perturbations of Galactic objects produced by a spiral density wave (Lin and Shu 1964) are described by the relations

$$V_R = -f_R \cos \chi, \quad (1)$$

$$\Delta V_\theta = f_\theta \sin \chi, \quad (2)$$

where

$$\chi = m[\cot(i) \ln(R/R_\odot) - \theta] + \chi_\odot \quad (3)$$

is the phase of the spiral density wave;  $m$  is the number of spiral arms;  $i$  is the pitch angle;  $\chi_\odot$  is the phase of the Sun in the spiral density wave (Rohlfs 1977);  $R_\odot$  is the Galactocentric distance of the Sun;  $\theta$  is the object's position angle:  $\tan \theta = y/(R_\odot - x)$ , where  $x$ ,  $y$  are the Galactic heliocentric rectangular coordinates of the object;  $f_R$  and  $\Delta f_\theta$  are the amplitudes of the radial and tangential perturbation components, respectively;  $R$  is the distance of the object from the Galactic rotation axis, which is calculated using the heliocentric distance  $r = 1/\pi$ :

$$R^2 = r^2 \cos^2 b - 2R_\odot r \cos b \cos l + R_\odot^2,$$

where  $l$  and  $b$  are the Galactic longitude and latitude of the object, respectively.

Equation (3) for the phase can be expressed in terms of the perturbation wavelength  $\lambda$ , which is equal to the distance between the neighboring spiral arms along the Galactic radius vector. The following relation is valid:

$$\frac{2\pi R_o}{\lambda} = m \cot(i). \quad (4)$$

Equation (3) will then take the form

$$\chi = \frac{2\pi R_o}{\lambda} \ln(R/R_o) - m\theta + \chi_\odot. \quad (5)$$

Here, we will consider only the radial velocities and, accordingly, the perturbations described by Eq. (1), because determining the residual tangential velocities with the needed accuracy to study the perturbations (2) is a rather complex task (especially in the case of a small number of objects) that requires constructing a smooth rotation curve with the highest accuracy. In contrast, the radial velocities do not depend on the rotation curve. The question of determining the residual velocities is considered below. The goal of our spectral analysis of the series of measured velocities  $V_{R_n}$ ,  $n = 1, 2, \dots, N$ , where  $N$  is the number of objects, is to extract the periodicity in accordance with model (1) describing a spiral density wave with parameters  $f_R$ ,  $\lambda$ , and  $\chi_\odot$ . If the wavelength  $\lambda$  is known, then the pitch angle  $i$  is easy to determine from Eq. (4) by specifying the number of arms  $m$ . Here, we adopt a two-armed model, i.e.,  $m = 2$ .

## 2.2 Spectral Analysis of the Perturbations

### 2.2.1 The linear approximation

The linear approximation for the logarithm of the argument for  $|R - R_o| \ll R_o$  and a small  $\theta$  can be represented as

$$\frac{2\pi R_o}{\lambda} \ln(R/R_o) \approx \frac{2\pi(R - R_o)}{\lambda}. \quad (6)$$

In this case, for our harmonic analysis of the velocities, we can apply the standard Fourier transform

$$\bar{V}_{\lambda_k} = \frac{1}{N} \sum_{n=1}^N V_{R_n} \exp\left(-j \frac{2\pi}{\lambda_k} (R_n - R_o)\right), \quad (7)$$

where  $\bar{V}_{\lambda_k}$  is the  $k$ th harmonic of the Fourier transform,  $V_{R_n}$  are the velocity measurements for objects with Galactocentric distances  $R_n$ ,  $n = 1, 2, \dots, N$ , and  $\lambda_k$  is the wavelength of the  $k$ -th harmonic, which is equal to  $D/k$ , where  $D$  is the period of the series being analyzed.

Since we are interested only in the perturbation power spectrum  $|\bar{V}_{\lambda_k}|^2$ , Eq. (7) can be simplified as follows:

$$\bar{V}_{\lambda_k} = \frac{1}{N} \sum_{n=1}^N V_{R_n} \exp\left(-j \frac{2\pi}{\lambda_k} R_n\right). \quad (8)$$

We used the latter expression previously (see Bobylev et al. 2008; Bobylev and Bajkova 2010) for our spectral analysis of the residual velocities for Galactic objects.

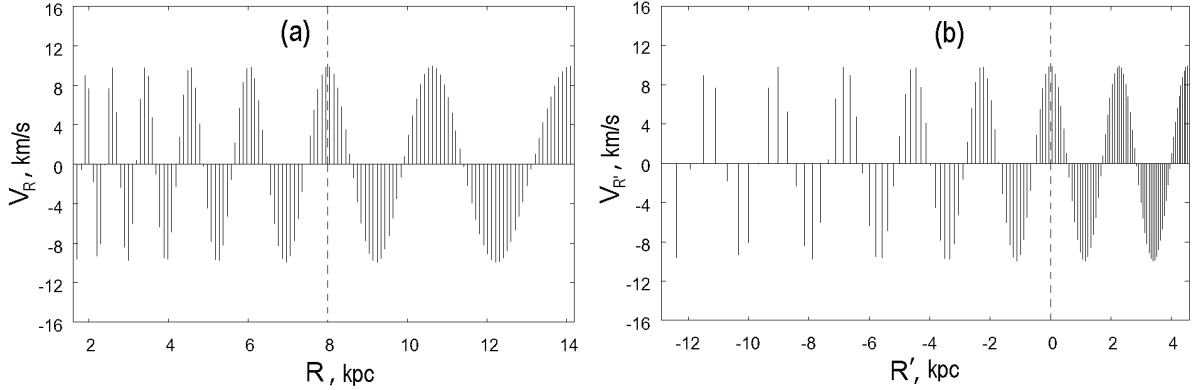


Рис. 1: Illustration of the change of variables when analyzing the perturbations as a function of the logarithm of the distances.

### 2.2.2 Analysis of the perturbations as functions of the logarithm of the distances.

Let us analyze the perturbations as a periodic function of the logarithm of the Galactocentric distances, for the time being, without allowance for the position angles of the objects:

$$\bar{V}_{\lambda_k} = \frac{1}{N} \sum_{n=1}^N V_{R_n} \exp\left(-j \frac{2\pi R_o}{\lambda_k} \ln(R_n/R_o)\right). \quad (9)$$

Obviously, if we make the change of variables

$$R'_n = \ln(R_n/R_o)R_o, \quad (10)$$

then Eq. (9) is reduced to the standard Fourier transform

$$\bar{V}_{\lambda_k} = \frac{1}{N} \sum_{n=1}^N V_{R'_n} \exp\left(-j \frac{2\pi R'_n}{\lambda_k}\right). \quad (11)$$

Figure 1 gives an illustration of this change, when the periodic function of the logarithm of  $R$  (Fig. 1a) turns into a periodic function of the new variable  $R'$  (Fig. 1b), which can already be analyzed using the standard Fourier transform.

Below, in the “Simulation Results” Section, we will show how important an accurate allowance for the logarithmic pattern of the spiral density wave is, especially when the objects are distributed in a wide range of Galactocentric distances.

### 2.2.3 Allowance for the position angles of the objects

Allowance for the position angles of the objects is a much more complex algorithmic problem. Let us represent Eq. (3) for the phase as

$$\chi = \chi_1 - m\theta, \quad (12)$$

where

$$\chi_1 = \frac{2\pi R_o}{\lambda} \ln(R/R_o) + \chi_\odot. \quad (13)$$

Substituting (12) into Eq. (1) for the perturbations at the  $n$ th point and performing standard trigonometric transformations, we will obtain

$$\begin{aligned} V_{R_n} &= f_R \cos(\chi_{1_n} - m\theta_n) \\ &= f_R \cos \chi_{1_n} \cos m\theta_n + f_R \sin \chi_{1_n} \sin m\theta_n \\ &= f_R \cos \chi_{1_n} (\cos m\theta_n + \tan \chi_{1_n} \sin m\theta_n). \end{aligned} \quad (14)$$

Let us designate

$$V'_R = f_R \cos \chi_1, \quad (15)$$

Owing to the substitution (15), it then follows from (14) that

$$V_{R_n} = V'_{R_n} (\cos m\theta_n + \tan \chi_{1_n} \sin m\theta_n). \quad (16)$$

Using Eq. (16), let us form a new data series

$$V'_{R_n} = V_{R_n} / (\cos m\theta_n + \tan \chi_{1_n} \sin m\theta_n), \quad (17)$$

to which a Fourier analysis can be applied in accordance with (11).

Thus, taking into account both the logarithmic pattern of the spiral density wave and the position angles of the objects, we obtain the following expression for our spectral analysis of the perturbations:

$$\bar{V}_{\lambda_k} = \frac{1}{N} \sum_{n=1}^N V'_{R'_n} \exp\left(-j \frac{2\pi R'_n}{\lambda_k}\right). \quad (18)$$

#### 2.2.4 The practical algorithm

The algorithm for realizing (18) consists of the following steps:

1. The initial series of velocities  $V_{R_n}$  is transformed into the series  $V'_{R'_n}$  in accordance with (10).

2. The power spectrum of the derived sequence  $V'_{R'_n}$  is calculated based on the Fourier transform (11) to obtain an estimate of  $\lambda_{max}$  that corresponds to the peak of the derived power spectrum.

3. A comb of several  $\lambda_i (i = 1, \dots, K)$  with a central  $\lambda_{max}$  is then specified.

The following iterations are made for each  $\lambda_i$  from the specified comb:

1) The value of  $\lambda_i$  and the initial approximation  $\chi_\odot$  (for example, equal to zero) are substituted into Eq. (13) to calculate  $\chi_1$  for each data reading ( $n = 1, \dots, N$ ).

2) Using Eq. (17), the series of velocities  $V'_{R'_n}$  is transformed into the series  $V''_{R'_n}$ . This transformation needs to be regularized to avoid the division by numbers close to zero. This is done by assigning a threshold number, say,  $\epsilon$ , and permission for the division is given only when the denominator in Eq. (17) exceeds this number. The best  $\epsilon$  at which the significance of the extracted peak in the spectrum reaches its maximum as a result of the iterations at the minimum residual between the solution and the data can be found

by an exhaustive search for  $\varepsilon$  from some interval. The typical values of  $\varepsilon$  found on model problems lie within the range  $[0.01, 0.3]$ .

3) The power spectrum of the derived sequence  $V'_{R'_n}$  is calculated based on the Fourier transform (18) to obtain a new estimate of  $\chi_{\odot}$  corresponding to a fixed  $\lambda_i$  of the derived power spectrum.

4) The return to the first step is made until the process will converge or diverge.

5) If the process converged, then we fix the specified  $\lambda_i$  and the derived  $\chi_{\odot}$ ; if it diverged, then we take the next value  $\lambda_{i+1}$  from the specified comb and make iterations (1)–(4) until the value of  $\lambda$  at which the process converges will be found.

4. The power spectrum is calculated for the values of  $\lambda$  and  $\chi_{\odot}$  found in accordance with (18) with the goal of a further analysis.

The above algorithm is basically interactive and can be efficiently applied to process the individual data realizations. In contrast, in the case of mass data processing, for example, during Monte Carlo simulations (see below), automation of the search for periodicities is required. For this purpose, we propose a slight modification of the algorithm described above that consists in seeking for the best solution by maximizing some criterion for the quality of signal extraction from noise. As such a criterion, we propose a parameter  $Q$  proportional to the peak value of the power spectrum  $S_{peak}$  and its significance  $p_{peak}$  (see the next subsection) and inversely proportional to the value of the maximum side lobe in the power spectrum  $S_{sidelobe}$  and the residual between the extracted periodic signal and the input data  $\delta$ , i.e., we suggest finding

$$\max Q = \frac{S_{peak} \times p_{peak}}{S_{sidelobe} \times \delta}$$

by varying  $\lambda_i (i = 1, \dots, K)$  and  $\varepsilon_j (j = 1, \dots, L)$ .

As a result, as the solution we take the values of the parameters  $\lambda$ ,  $f_R$  and  $\chi_{\odot}$  at which  $Q$  reaches its maximum. Note that the solution for  $f_{R_i}$  for each  $\lambda_i$  is sought from the condition for the residual between the extracted harmonic and the input data being at its minimum.

The high robustness of the constructed algorithm was established through numerous simulations of the extraction of a harmonic signal from noise at various numbers and various sampling intervals of data, various signal-to-noise ratios, and various degrees of nonuniformity of the data series.

### 2.2.5 The criterion for extracting a harmonic signal from noise

Since we actually solve the problem of extracting a harmonic signal from noise, statistical criteria for separating the signal and noise components should be applied. Here, we use a well-known criterion based on Schuster's theorem (Vityazev 2001). It consists in specifying a positive number  $q \ll 1$  that defines the probability (significance level) of a very rare event—the appearance of a strong peak in the power spectrum (periodogram) of white noise. In the case where the frequency of the periodic component is not known in advance, it is quite natural to assume that the largest value of the periodogram  $|\bar{V}_{\lambda_k}|^2_{max}$  corresponds to the sought-for periodic component. If the following inequality holds:

$$|\bar{V}_{\lambda}|^2_{max} \geq \frac{\sigma_0^2}{N} X,$$

where

$$\begin{aligned}\sigma_0^2 &= \frac{1}{N-1} \sum_{n=1}^N (V_{R_n} - \bar{V})^2, \\ \bar{V} &= \frac{1}{N} \sum_{n=1}^N V_{R_n}, \\ X &= -\ln(1 - (1 - q)^{2/(N-2)}),\end{aligned}$$

then the assertion that  $|\bar{V}_\lambda|_{max}^2$  belongs to the signal and not to the noise is adopted with the probability  $p = 1 - q$ .

### 2.2.6 Monte Carlo simulations

We use statistical Monte Carlo simulations to estimate the errors of the parameters being determined. In accordance with this method, we generate  $M$  independent realizations of the velocities and coordinates for the objects by taking into account their random measurement errors that are known to us.

We assume that the data measurement errors are distributed according to a normal law with a mean equal to the nominal value and a dispersion equal to  $\sigma_l = error_l$ ,  $l = 1, \dots, N_d$ , where  $N_d$  is the number of data and  $error_l$  designates the measurement error of a single measurement with number  $l$  (one sigma). Each element of a random realization is formed independently by adding the nominal value of the measured data with number  $l$  and a random number generated according to a normal law with a zero mean and dispersion  $\sigma_l$ . Note that the latter is limited from above by  $3\sigma_l$ .

Subsequently, each random realization of data with number  $j$  ( $j = 1, \dots, M$ ) formed in this way is processed according to the algorithm described above to determine the sought-for parameters  $f_R^j, \lambda^j, \chi_\odot^j$ . The means of the parameters and their dispersions are then determined from the derived sequences of estimates:  $m_{f_R} \pm \sigma_{f_R}, m_\lambda \pm \sigma_\lambda, m_{\chi_\odot} \pm \sigma_{\chi_\odot}$ . The statistical characteristics of the spiral density wave pitch angle  $i$  can be easily determined using Eq. (4):  $m_i \pm \sigma_i$ .

## 2.3 Spectrum Reconstruction by the Maximum Entropy Method

So far we have considered the simplest method of periodogram analysis for series. In the case where the data series are irregular, i.e., there are large gaps, the signal spectrum is distorted by large side lobes and it becomes difficult to distinguish the spectral component of the signal from spurious peaks. In this case, it may turn out to be useful to apply the methods of spectrum reconstruction from the available data. This problem is fundamentally resolvable if the sought for signal has a finite spectrum. Since our problem belongs to the class of problems on the extraction of polyharmonic functions from noise, we assume that this condition is met.

There are two main nonlinear methods for reconstructing both one-dimensional signals and images—these are the CLEAN method and the maximum entropy method (MEM). Here, we consider the MEM as a more fundamental method that has a rigorous logical justification (Jaynes 1968). Since the spectrum, i.e., a complex-valued function, is the

function to be reconstructed, we apply the generalized MEM (GMEM) described in detail by Bajkova (1992) and Frieden and Bajkova (1994).

We will use the following notation:

1. The input data of the series:  $V_n = V'_{R'_n}, n = 1, \dots, N$ , with coordinates  $l_n$  on a discrete mesh  $1, \dots, K = 2^\alpha$ ,  $\alpha$  is an integer,  $> 0$ ;

2. The discrete Fourier spectrum of the input data:  $X_k + jY_k, k = 1, \dots, K$ .

The spectrum and the data are related by the inverse Fourier transform

$$\frac{1}{K} \sum_{k=1}^K (X_k + jY_k) \exp\left(j \frac{2\pi(k-1)(l_n-1)}{K}\right) = V_n.$$

Given the Hermitian symmetry of the spectrum for a real-valued signal and the data measurement errors, the constraints on the unknowns can be rewritten as

$$\sum_{k=K_1}^{k=K_2} X_k a_{k,n} - Y_k b_{k,n} + \eta_n = V_n,$$

where  $a_{k,n} = \frac{2}{K} \cdot \cos\left(\frac{2\pi(k-1)(l_n-1)}{K}\right)$ ,  $b_{k,n} = \frac{2}{K} \cdot \sin\left(\frac{2\pi(k-1)(l_n-1)}{K}\right)$ ,  $\eta_n$  is the measurement error of the  $n$ th value of the series that obeys a random law with a normal distribution with a zero mean and dispersion  $\sigma_n$ .

In our case, the reconstruction problem consists in finding the maximum of the following generalized entropy functional:

$$E = - \sum_{k=K_1}^{k=K_2} X_k^+ \ln(aX_k^+) + X_k^- \ln(aX_k^-) + Y_k^+ \ln(aY_k^+) + Y_k^- \ln(aY_k^-) - \sum_{n=1}^{n=N} \frac{\eta_n^2}{\sigma_n^2},$$

where the sought-for variables  $X_k$  and  $Y_k$  are represented as the difference of the positive and negative parts:  $X_k = X_k^+ - X_k^-$  и  $Y_k = Y_k^+ - Y_k^-$ , respectively; in this case,  $X_k^+, X_k^-, Y_k^+, Y_k^- \geq 0$ ,  $a > 0$  is the real-valued parameter responsible for the separation of the positive and negative parts of the sought-for variables with the required accuracy (in our case, we adopted  $a = 1000$ ),  $K_1$  and  $K_2$  are the a priori known lower and upper localization boundaries of the sought-for finite spectrum.

## 2.4 Simulation Results

In this section, we present the results of testing our developed algorithms of spectral analysis based on both the Fourier transform and the series reconstruction using the GMEM (Fig. 2).

The data series were formed in accordance with the relation describing the spiral density wave (see also (1) and (5)):

$$V_{R_n} = f_R \cos\left(\frac{2\pi R_o}{\lambda} \ln(R_n/R_o) - m\theta_n + \chi_\odot\right) + \eta_n, \quad n = 1, \dots, N,$$

where  $\eta_n$  is additive white noise with a normal distribution law with dispersion  $\sigma$  and a zero mean.



We adopted the following model parameters: the perturbation amplitude of the spiral density wave  $f_R = 10 \text{ km s}^{-1}$ ; the perturbation wavelength  $\lambda = 2.1 \text{ kpc}$ ; the Galactocentric distance of the Sun  $R_\odot = 8 \text{ kpc}$ ; the number of spiral arms  $m = 2$ ; the Sun’s phase in the spiral density wave  $\chi_\odot = 90^\circ$ ; the number of objects  $N = 44$  (taken to be equal to the number of Galactic masers whose velocities are analyzed below); the position angles  $\theta_n$  of the objects were specified randomly in accordance with a uniform distribution law within the range  $[-\pi/4, \pi/4]$ . The power spectrum of such a signal in the absence of noise consists of a single peak with an amplitude  $f_R^2/4 = 25 \text{ km}^2 \text{ s}^{-2}$ . The signal-to-noise ratio of the model data was 2.63.

The initial model sequence of radial velocities  $V_{R_n}$  is shown in Fig. 2a. It differs from the strictly harmonic one due to the scatter of position angles for the objects and the measurement errors. The range of Galactocentric distances is from 1.5 to 17 kpc. The sequence of velocities  $V_{R'_n}$  derived in accordance with Eq. (10), which transforms the logarithmic distances into the linear ones, is shown in Fig. 2b. The vertical dashed line in the figures passes through the point corresponding to the Galactocentric distance of the Sun.

To be able to apply fast computational algorithms (fast Fourier transform), we represented our data as a discrete sequence on a uniform mesh  $\mathbf{N} = 2^{14}$  pixels in size and took the size of a single pixel to be 0.005 kpc to provide data pixelization with the required accuracy (in order that no more than one measurement fall into one pixel) and to obtain the highest-resolution spectrum. As a result, the length of the analyzed period for the discrete sequence was  $D = \mathbf{N} \times 0.005 = 81.92 \text{ kpc}$ . Obviously, the values of the  $\mathbf{N}$ -point sequence are taken to be zero in the pixels into which no data fall.

The power spectrum of the initial sequence  $V_{R_n}$  calculated (in accordance with the linear approximation of the logarithm of the argument (6)) using the Fourier transform (8) is shown in Fig. 2d. It is difficult to extract the significant peak corresponding to the model signal from this spectrum. Consequently, the linear approximation (6) is not satisfactory in our case.

The power spectrum of the sequence  $V_{R'_n}$  calculated from (11) is shown in Fig. 2e. We see from this figure that taking into account the logarithmic pattern of the spiral density wave (we have not yet taken the maser position angles into account) allowed a significant peak with an amplitude of  $10 \text{ km}^2 \text{ s}^{-2}$  to be extracted at the required wavelength  $\lambda = 2.1 \text{ kpc}$ , which, however, is a factor of 2.5 lower than the theoretical one. The probability that the peak belongs to the signal and not to the noise at the level indicated by the horizontal dashed line is  $p = 0.95$ . (The dashed line here and in similar figures is drawn at 3/4 of the maximum value of the periodogram.) The sought-for harmonic of the perturbations corresponding to the peak and having the smallest residual with the data is indicated by the dotted line in Fig. 2b. Its amplitude is  $f_R = 7 \text{ km s}^{-1}$ . The Sun’s phase in the spiral density wave is  $\chi_\odot = 81.2^\circ$ .

Allowance for both the logarithmic pattern of the spiral density wave and the position angles of the objects according to the scheme described in the “Practical algorithm” Section led to the result shown in Figs. 2c and 2f. It can be seen from Fig. 2c how noticeably the envelope of the velocities changed once the position angles had been taken into account: the values now fit almost exactly into the harmonic signal indicated by the dashed line with an amplitude  $f_R = 10 \text{ km s}^{-1}$  and a wavelength  $\lambda = 2.1 \text{ kpc}$  corresponding to the

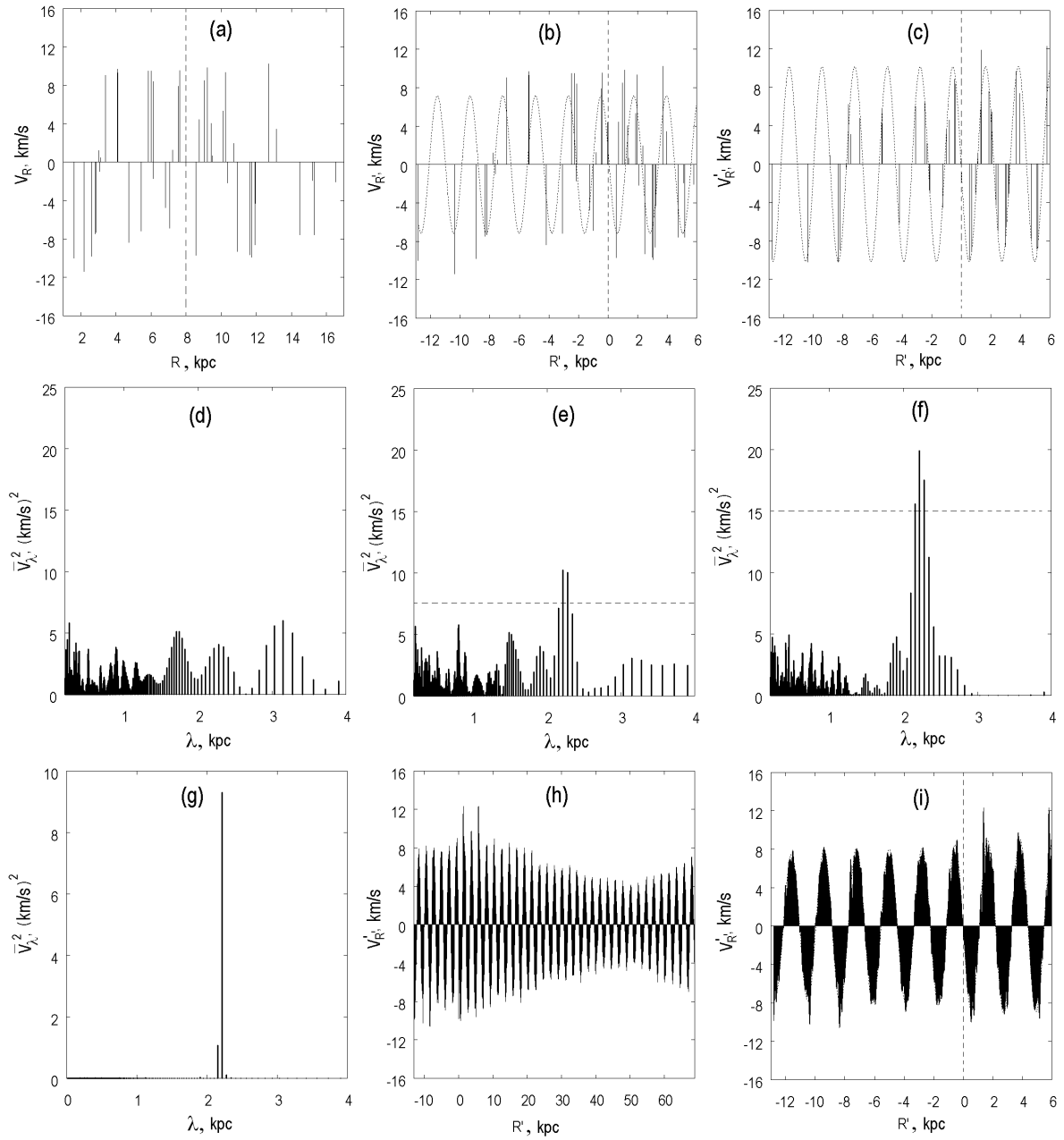


Рис. 2: Simulation results.

peak in the power spectrum of the reconstructed signal (Fig. 2f). The amplitude of the peak is  $20 \text{ km}^2 \text{ s}^{-2}$ , which is twice that in the preceding case. The significance of the peak at the level indicated by the horizontal dashed line is  $p = 0.99997$ . The Sun’s phase in the spiral density wave is  $\chi_{\odot} = 92^{\circ}$ .

To determine the range of possible solutions, i.e., the errors in the parameters, we performed Monte Carlo simulations (see the “Monte Carlo Simulations” Section). We generated  $M = 1000$  random realizations of data by varying their values within the limits of measurement errors obeying a normal law. Having applied our method of searching for periodicities to the simulated realizations of data, we obtained the means and dispersions of the spiral density wave parameters ( $m_{par} \pm \sigma_{par}$ ): the perturbation amplitude  $f_R = 7.4 \pm 1.3 \text{ km s}^{-1}$ , the perturbation wavelength  $\lambda = 2.2 \pm 0.1 \text{ kpc}$ , the pitch angle of the spiral density wave  $i = -5.15^{\circ} \pm 0.15^{\circ}$ , and the Sun’s phase in the spiral density wave  $\chi_{\odot} = 87^{\circ} \pm 20^{\circ}$ . Note that the means of the parameters turned out to be slightly shifted relative to the values corresponding to the nominal data.

Thus, using the proposed iterative scheme of periodogram analysis, we managed to reconstruct the spiral density wave parameters from the model radial velocities of 44 objects having a wide scatter in both Galactocentric distances and position angles with a sufficiently high accuracy. Clearly, the accuracy of determining the spiral density wave parameters increases with increasing number of objects and increasing accuracy of measuring their coordinates and velocities.

As has already been said in the previous section, large side lobes can be obtained in the case of large gaps in the data, which can make it difficult to separate the signals of real and spurious peaks in the periodogram. A spectral analysis with the application of series reconstruction methods makes it possible to increase the significance of extracting the useful signal. The reconstruction results based on the GMEM as applied to the  $V'_{R'_n}$ , data obtained by applying an iterative periodogram analysis are shown in Figs. 2g, 2h, and 2i. Figures 2h and 2i show the reconstructed sequence  $V'_{R'_n}$  on the entire analyzed period and in the region of data from  $-12.82 < R' < 5.8 \text{ kpc}$ . It can be seen from Fig. 2g, where the reconstructed spectrum is shown, that we managed to get rid of the side lobes seen in Figs. 2f almost completely and, thus, to increase the significance of extracting the periodic signal ( $p = 1$ ), determining its wavelength, and the Sun’s phase in the spiral density wave. Since we failed to reconstruct the signal outside the range containing the data (Fig. 2h) with a high accuracy, this led to a decrease in the amplitude of the spectral peak in Fig. 2g. Nevertheless, we managed to obtain accurate values of such parameters as the wavelength  $\lambda = 2.1 \text{ kpc}$  and the Sun’s phase  $\chi_{\odot} = 90^{\circ}$ .

### 3 ANALYSIS OF MASERS

#### 3.1 Data

Previously (Bobylev and Bajkova 2010; Stepanishchev and Bobylev 2011), we analyzed a sample of 28 masers with measured trigonometric parallaxes, proper motions, and line-of-sight velocities drawn from published data. By now, the amount of such data has increased considerably—about 20 new measurements in various regions of active star formation have

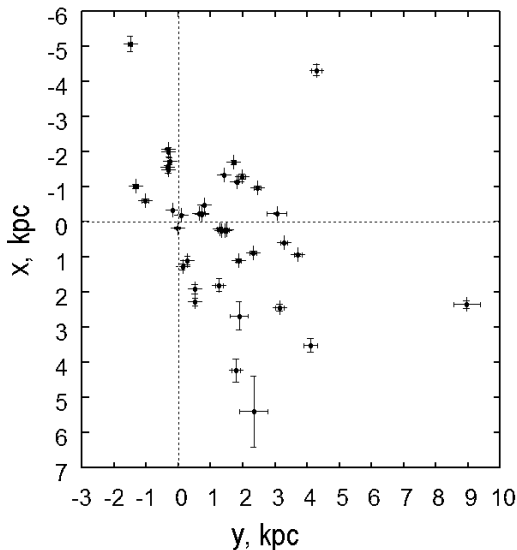


Рис. 3: Maser positions in projection onto the Galactic  $xy$  plane (the Sun is at the coordinate origin).

been published. The initial data on 44 masers associated with the youngest Galactic stellar objects (either protostellar objects of various masses, or very massive supergiants, or T Tau stars) are given in the table.

The observational data, namely the trigonometric parallaxes and proper motions of the objects, were obtained by several research groups through longterm radio-interferometric observations within the framework of various projects. One of them is the Japanese VERA (VLBI Exploration of Radio Astrometry) project on the observation of Galactic H<sub>2</sub>O masers at 22 GHz and SiO masers (there are very few such sources among young objects) at 43 GHz. Note that the higher the frequency, the higher the resolution, the more accurate the observations. Methanol (CH<sub>3</sub>OH) masers are observed at 12 GHz on the VLBA (NRAO). The radio-interferometric observations of radio stars in continuum at 8.4 GHz are being carried out with the same goals.

Several radio-interferometric determinations of the parallaxes and proper motions have been made for a number of objects in the Orion Nebula. These include SiO masers (Kim et al. 2008), H<sub>2</sub>O masers (Hirota et al. 2007), radio observations of the radio star GMR A (a low-mass T Tau star) at 15 GHz (Sandstrom et al. 2007), and independent observations of several radio stars at 8.4 GHz (Menten et al. 2007). Menten et al. (2007) deduced the mean parallax and proper motion from four radio stars in the cluster of the Orion Nebula: GMR A, GMR 12, GMR F, and GMR G. In the opinion of Kim et al. (2008), the SiO masers are associated with the accretion disk rotating around the source “N” in the central region of Orion/KL. According to Goddi et al. (2011), this radio source is a binary system with a total mass of  $\approx 20M_{\odot}$ . Note that the proper motions from different measurements differ significantly. Therefore, we used two independent measurements indicated in the table.

The star YV CMa, a red supergiant with a mass of  $\approx 25M_{\odot}$  and an age of  $\approx 8$  Myr,

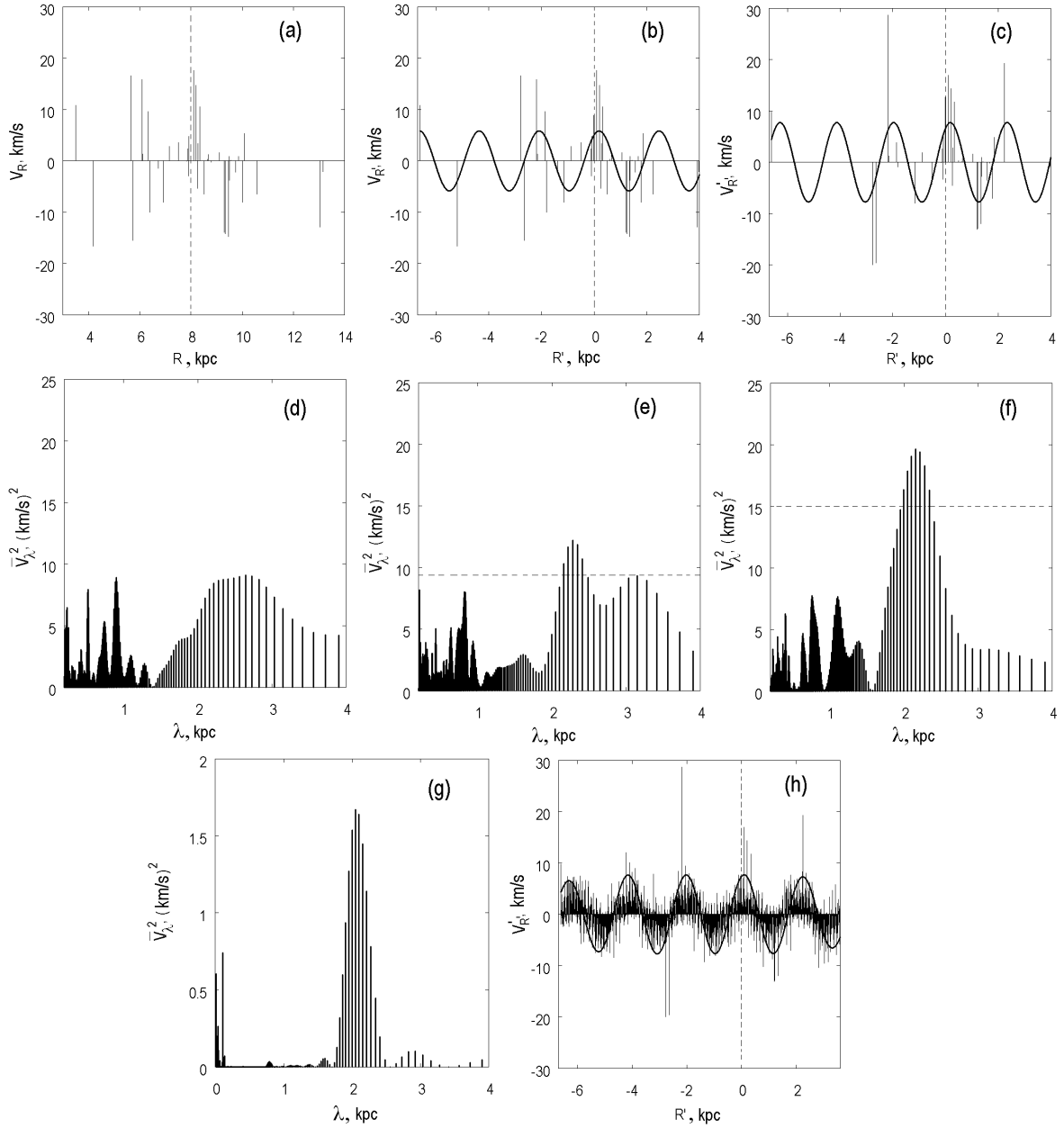


Рис. 4: Results of processing the data on 44 masers.

is surrounded by a thick expanding envelope (Zhang et al. 2012). The red supergiant S Per is also surrounded by an expanding envelope (Asaki et al. 2010).

In the star-forming region G5.89–0.39, the water masers that were used to determine the trigonometric parallax are associated with the accretion disk located inside an ultracompact HII region, which is at the expansion stage itself (Motogi et al. 2011). The gas is ionized by a just born massive  $\approx 0.8$  star. An overview of the complex picture in this region can be found in Xu et al. (2012).

In the star-forming region Cep A, we use both observations of methanol masers at 12 GHz (Moscadelli et al. 2009) for the source HW2 (a massive protostellar object) and independent continuum observations of the radio source HW9 (this is either a T tau star or a young Ae/Be star with a mass of less than  $6M_{\odot}$ ) at 8.4 GHz (Dzib et al. 2011).

In the star-forming region NGC 1333, we averaged the proper motions of two maser features, f1 and f2, that are associated with the young stellar object SVS 13 (Hirota et al. 2008a). New data (Hirota et al. 2011) on the young stellar object with clear evidence of a bipolar jet have been obtained in this region associated with the molecular cloud Lynds 1448 C in Perseus.

The line-of-sight velocities  $V_r$  ( $LSR$ ) in the table are given relative to the Local Standard of Rest. Their values were determined by different authors from radio observations in CO lines. Occasionally, the cited authors do not provide the error in the line-of-sight velocity; we then took it to be  $5 \text{ km s}^{-1}$ .

As follows from the table, on average, the parallaxes were determined with a relative error  $\sigma_{\pi}/\pi \approx 5\%$ , and only in three regions does it exceed appreciably the mean level. These are IRAS 16293-2422 ( $\sigma_{\pi}/\pi = 19\%$ ), G 23.43-0.20 ( $\sigma_{\pi}/\pi = 18\%$ ) and W 48 ( $\sigma_{\pi}/\pi = 14\%$ ).

The distribution of masers in projection onto the Galactic  $xy$  plane is shown in Fig. 3, from which we see a fairly wide scatter in coordinates  $x, y$  and, hence, in position angles in the Galactic  $xy$  plane.

## 3.2 Results and Discussion

First of all, we redetermined the parameters of the Galactic rotation curve from the data on 44 masers. Our technique, which is based on the expansion of the angular velocity of Galactic rotation in a Taylor series of the Galactocentric distance  $R$ , was described in detail previously (see Bobylev and Bajkova 2010; Stepanishchev and Bobylev 2011).

At fixed  $R_0 = 8 \text{ kpc}$ , we obtained the components of the peculiar solar velocity  $(U_{\odot}, V_{\odot}, W_{\odot}) = (7.6, 17.8, 8.3) \pm (1.5, 1.4, 1.2) \text{ km s}^{-1}$  and the following Galactic rotation parameters:  $\Omega_0 = -28.8 \pm 0.8 \text{ km s}^{-1} \text{ kpc}^{-1}$ ,  $\Omega'_0 = +4.18 \pm 0.15 \text{ km s}^{-1} \text{ kpc}^{-2}$ ,  $\Omega''_0 = -0.87 \pm 0.06 \text{ km s}^{-1} \text{ kpc}^{-3}$ . The linear Galactic rotation velocity at  $R = R_0$  is then  $V_0 = |R_0\Omega_0| = 230 \pm 14 \text{ km s}^{-1}$ .

There is good agreement of our results with the results of analyzing masers by different authors. Based on a sample of 18 masers, McMillan and Binney (2010) showed that  $\Omega_0$  lying within the range  $29.9 - 31.6 \text{ km s}^{-1} \text{ kpc}^{-1}$  at various  $R_0$  was determined most reliably and obtained an estimate of  $V_0 = 247 \pm 19 \text{ km s}^{-1}$  for  $R_0 = 7.8 \pm 0.4 \text{ kpc}$ . Based on a sample of 18 masers, Bovy et al. (2009) found  $V_0 = 244 \pm 13 \text{ km s}^{-1}$  at  $R_0 = 8.2 \text{ kpc}$ . Using 28 masers, Stepanishchev and Bobylev (2011) found the following

Таблица 1: Initial data on the masers

Source	$\alpha$	$\delta$	$\pi(\sigma_\pi)$	$\mu_\alpha^*(\sigma_{\mu_\alpha})$	$\mu_\delta(\sigma_{\mu_\delta})$	$V_r(\sigma_{V_r})$	Ref
S252A	92.2222	21.6414	.476(.006)	.02(.01)	-2.02(.04)	10.8(3)	(1)
G232.6+0.99	113.0408	-16.9702	.596(.035)	-2.17(.06)	2.09(.46)	22.8(3)	(1)
Cep A	344.0754	62.0304	1.430(.080)	.50(1.1)	-3.70(.20)	-10.5(5)	(1)
NGC 7538	348.4390	61.4696	.378(.017)	-2.45(.03)	-2.44(.06)	-57.0(3)	(1)
V645	295.7969	23.7343	.463(.020)	-1.65(.03)	-5.12(.07)	27.4(3)	(1)
G35.20-0.74	284.5544	1.6766	.456(.045)	-.18(.08)	-3.63(.16)	27.9(3)	(1)
W48	285.4397	1.2257	.306(.045)	-.71(.07)	-3.61(.24)	41.9(3)	(1)
G23.43-0.20	278.6633	-8.5237	.170(.032)	-1.93(.10)	-4.11(.07)	97.6(3)	(1)
G23.01-0.41	278.6678	-9.0107	.218(.017)	-1.72(.04)	-4.12(.30)	81.5(3)	(1)
Orion	83.8098	-5.3773	2.425(.035)	3.30(1.0)	.10(1.0)	10.0(5)	(2)
Orion/KL	83.8104	-5.3751	2.390(.030)	9.56(.10)	-3.83(.15)	5.0(5)	(3)
W3 (OH)	36.7702	61.8735	.512(.007)	-1.20(.02)	-.15(.01)	-44.2(3)	(4)
IRAS 00420	11.2433	55.7799	.460(.010)	-2.52(.05)	-.84(.04)	-46.0(5)	(5)
IRAS 16293	248.0952	-24.4768	5.6(1.1)	-20.6(.7)	-32.4(2.0)	4.4(5)	(6)
NGC 1333	52.2655	31.2677	4.250(.320)	14.25(1.0)	-8.95(1.4)	7.5(5)	(7)
IRAS 22198	335.3614	63.8605	1.309(.047)	-3.00(.50)	.0(1.0)	-17.0(5)	(8)
S269	93.6544	13.8267	.189(.008)	-.42(.01)	-.12(.04)	19.6(3)	(9)
WB89-437	40.8690	62.9523	.164(.006)	-1.27(.05)	.82(.12)	-72.0(3)	(10)
L1287	9.1973	63.4839	1.077(.039)	-.86(.11)	-2.29(.56)	-23.5(3)	(11)
NGC 281-W	13.1008	56.5620	.421(.022)	-2.69(.16)	-1.77(.11)	-29.5(3)	(11)
S255	93.2251	17.9898	.628(.027)	-.14(.54)	-.84(1.76)	4.6(3)	(11)
L1206	337.2142	64.2281	1.289(.153)	.27(.23)	-1.40(1.95)	-12.0(3)	(11)
S Per	35.7155	58.5865	.413(.017)	-.49(.23)	-1.19(.20)	-38.5(1)	(12)
IRAS 06061	92.2791	21.8448	.496(.031)	-.10(.10)	-3.91(.07)	-1.6(5)	(13)
G14.33-0.64	274.7278	-16.7973	.893(.101)	.95(2.0)	-2.50(2.0)	22.0(10)	(14)
W51 Main/S	290.9328	14.5082	.185(.010)	-2.64(.16)	-5.11(.16)	58.0(4)	(15)
IRAS 06058	92.2229	21.6418	.569(.034)	1.06(.10)	-2.77(.20)	3.0(3)	(16)
IRAS 19213	290.9055	17.4862	.251(.010)	-2.53(.10)	-6.07(.30)	41.7(3)	(16)
AFGL 2789	324.9928	50.2392	.326(.032)	-2.20(.13)	-3.77(.36)	-44.0(3)	(16)
L1448C	51.4120	30.7348	4.31(.33)	21.90(.07)	-23.10(.33)	4.5(5)	(17)
G 5.89-0.39	270.1263	-24.0679	.780(.050)	.17(.10)	-.95(.10)	10.0(3)	(18)
Onsala 1	302.5383	31.5267	.404(.017)	-3.10(.18)	-4.70(.24)	12.0(1)	(19)
Onsala 2N	305.4334	37.6104	.261(.009)	-2.79(.13)	-4.66(.17)	.0(1)	(20)

Table 1 (Continue)

Source	$\alpha$	$\delta$	$\pi(\sigma_\pi)$	$\mu_\alpha^*(\sigma_{\mu_\alpha})$	$\mu_\delta(\sigma_{\mu_\delta})$	$V_r(\sigma_{V_r})$	Ref
G192.1-3.8	89.5564	16.5330	.660(.040)	.69(.15)	-1.57(.15)	5.7(3)	(21)
G12.9+0.45	272.9642	-17.5250	.428(.022)	.16(.03)	-1.90(1.59)	39.8(5)	(22)
M17	275.1034	-16.1931	.505(.033)	.68(.05)	-1.42(.09)	23.4(5)	(22)
G75.3+1.32	304.0667	37.5961	.108(.005)	-2.37(.09)	-4.48(.17)	-57.0(2)	(23)
W75N	309.6518	42.6263	.772(.042)	-1.97(.10)	-4.16(.15)	9.0(5)	(24)
DR21	309.7529	42.3806	.666(.035)	-2.84(.15)	-3.80(.22)	-3.0(5)	(24)
DR20	309.2540	41.5821	.687(.038)	-3.29(.13)	-4.83(.26)	-3.0(5)	(24)
IRAS 20290	307.7111	41.0410	.737(.062)	-2.84(.09)	-4.14(.54)	-1.4(5)	(24)
AFGL 2591	307.7111	41.0410	.300(.010)	-1.21(.32)	-4.80(.12)	-5.7(5)	(24)
HW9 CepA	344.0777	62.0300	1.43(.07)	-.76(.11)	-1.85(.04)	-10.5(5)	(25)
VY CMa	110.7430	-25.7675	.830(.080)	-2.80(.20)	2.60(.20)	18.0(3)	(26)

Note.  $\alpha$  and  $\delta$  in degrees,  $\pi$  is in mas,  $\mu_\alpha^* = \mu_\alpha \cos \delta$  and  $\mu_\delta$  is in mas yr<sup>-1</sup>,  $V_r = V_r(LSR)$  is in km s<sup>-1</sup>; the numbers mark the references to papers: (1) Reid et al. (2009); (2) Menten et al. (2007); (3) Kim et al. (2008); (4) Xu et al. (2006); (5) Moellenbrock et al. (2009); (6) Imai et al. (2007); (7) Hirota et al. (2008a); (8) Hirota et al. (2008b); (9) Honma et al. (2007); (10) Hachisuka et al. (2009); (11) Rygl et al. (2010); (12) Asaki et al. (2010); (13) Niinuma et al. (2011); (14) Sato et al. (2010a); (15) Sato et al. (2010b); (16) Oh et al. (2010); (17) Hirota et al. (2011); (18) Motogi et al. (2011); (19) Nagayama et al. (2011); (20) Ando et al. (2011); (21) Shiozaki et al. (2011); (22) Xu et al. (2011); (23) Sanna et al. (2012); (24) Rygl et al. (2011); (25) Dzib et al. (2011); (26) Zhang et al. (2012).



parameters:  $(U_{\odot}, V_{\odot}, W_{\odot}) = (8.5, 17.1, 8.9) \pm (1.6, 1.6, 1.6) \text{ km s}^{-1}$ , и  $\Omega_0 = -30.4 \pm 0.7 \text{ km s}^{-1} \text{ kpc}^{-1}$ ,  $\Omega'_0 = 4.23 \pm 0.13 \text{ km s}^{-1} \text{ kpc}^{-2}$ ,  $\Omega''_0 = -1.01 \pm 0.06 \text{ km s}^{-1} \text{ kpc}^{-3}$ .

It is important that the rotation-curve parameters found are in good agreement with the results of analyzing young Galactic disk objects rotating most rapidly around the center: OB associations with  $\Omega_0 = -31 \pm 1 \text{ km s}^{-1} \text{ kpc}^{-1}$  (Mel'nik et al. 2001; Mel'nik and Dambis 2009), blue supergiants with  $\Omega_0 = -29.6 \pm 1.6 \text{ km s}^{-1} \text{ kpc}^{-1}$  and  $\Omega'_0 = 4.76 \pm 0.32 \text{ km s}^{-1} \text{ kpc}^{-2}$  (Zabolotskikh et al. 2002), or OB3 stars with  $\Omega_0 = -31.5 \pm 0.9 \text{ km s}^{-1} \text{ kpc}^{-1}$ ,  $\Omega'_0 = +4.49 \pm 0.12 \text{ km s}^{-1} \text{ kpc}^{-2}$  and  $\Omega''_0 = -1.05 \pm 0.38 \text{ km s}^{-1} \text{ kpc}^{-3}$  (Bobylev and Bajkova 2011).

The Galactocentric radial,  $V_{R_n}$ , and tangential,  $V_{\theta_n}$  ( $n = 1, \dots, 44$ ,) velocities of the masers were determined from the relations

$$V_{\theta_n} = U_n \sin \theta_n + (V_0 + V_n) \cos \theta_n, \quad (19)$$

$$V_{R_n} = -U_n \cos \theta_n + (V_0 + V_n) \sin \theta_n, \quad (20)$$

where  $U_n, V_n$  are the heliocentric space velocities freed from the peculiar solar velocity  $U_{\odot}, V_{\odot}$  found.

The residual tangential velocities are obtained from the tangential velocities (19) minus the smooth rotation curve that is defined by the Galactic rotation parameters  $\Omega_0, \Omega'_0$ , and  $\Omega''_0$  found. The radial velocities (20) depend only on one Galactic parameter  $\Omega_0$  and do not depend on the rotation curve. As our experience showed (Bobylev and Bajkova 2010), the data are so far insufficient to reliably extract the density wave from the tangential residual velocities of the masers. Therefore, here we determine the spiral density wave parameters only from the radial velocities.

The results of our processing of the radial velocities are presented in Fig. 4. The length of the discrete sequence and the pixelization parameters were chosen to be the same as those in the case of our simulations (see the ‘‘Simulation Results’’ Section). Figure 4a shows the initial sequence of velocities  $V_{R_n}, n = 1, \dots, 44$ . We see that the Galactocentric distances occupy a fairly wide range, from 3.5 to 13.2 kpc. The sequence of velocities  $V_{R'_n}$  derived in accordance with Eq. (10), which transforms the logarithmic distances into the linear ones, is shown in Fig. 4b. The power spectrum of the initial sequence  $V_{R_n}$  that we calculated based on the Fourier transform (8) is shown in Fig. 4d. We see from this figure that at least four peaks have comparable significances and none of them can be extracted as the main one. The peak near 2 kpc is too blurred to determine the corresponding wavelength with an acceptable accuracy. Hence it follows that it is inappropriate to use the linear approximation (6) to analyze our data.

The power spectrum of the transformed sequence  $V_{R'_n}$ , calculated using (11) is shown in Fig. 4e. We see from this figure that taking into account the logarithmic pattern of the spiral density wave allowed a significant ( $p = 0.83$ ) peak equal to  $12.2 \text{ km}^2 \text{ s}^{-2}$ . The harmonic corresponding to this peak and having the smallest residual with the data is indicated in Fig. 4b by the solid line. Its amplitude is  $f_R = 5.8 \text{ km s}^{-1}$ . The Sun's phase in the spiral density wave measured from the center of the Carina–Sagittarius arm (Rohlf 1977) ( $R \approx 7 \text{ kpc}$ ) is  $\chi_{\odot} = -149^\circ$ .

Allowance for both the logarithmic pattern of the spiral density wave and the position angles of the objects according to the scheme described in the ‘‘Practical algorithm’’ Section

led to the result shown in Figs. 4c and 4f. It can be seen from Fig. 4c that the sequence of velocities  $V'_{R'_n}$  was modified noticeably compared to  $V_{R'_n}$  in Fig. 4b, fitting more closely into the harmonic signal (solid line) corresponding to the largest peak in the power spectrum (Fig. 4f). The perturbation amplitude is  $f_R = 7.7 \text{ km s}^{-1}$  and the wavelength is  $\lambda = 2.2 \text{ kpc}$ . The Sun's phase in the spiral density wave is  $\chi_\odot = -147^\circ$ . The amplitude of the peak in the power spectrum is  $20 \text{ km}^2 \text{ s}^{-2}$ , which is almost twice as high as that in the previous case. The significance of the peak at the level indicated by the horizontal dashed line in Fig. 4f is  $p = 0.98$ , while the significance level of the peak in the spectrum (Fig. 4e) is only  $p = 0.83$ .

The results of our reconstruction using the GMEM as applied to the  $V'_{R'_n}$  data obtained during an iterative periodogram analysis are shown in Figs. 4g and 4h. Figure 4g presents the reconstructed power spectrum, while Fig. 4h presents the reconstructed data series together with the extracted periodic signal (solid line) corresponding to the peak in the power spectrum and constituting the minimum residual with the initial  $V'_{R'_n}$ . As we see from Fig. 4g, using the GMEM-based spectrum reconstruction method allowed us to get rid of the side lobes near the main peak almost completely and, thus, to increase considerably the significance of the extracted periodicity ( $p = 1$ ) with  $\lambda = 2.2 \text{ kpc}$ . The discrepancy between the extracted periodic signal and the reconstructed sequence  $V'_{R'_n}$  (Fig. 4h) is high-frequency noise in the wavelength range  $0 < \lambda < 0.11 \text{ kpc}$  (see Fig. 4g), which is of no interest for our problem.

Based on our Monte Carlo simulations of 1000 random data realizations by varying their values within the limits of measurement errors obeying a normal distribution law, we obtained the means and dispersions of the spiral density wave parameters ( $m_{par} \pm \sigma_{par}$ ): the perturbation amplitude  $f_R = 7.8 \pm 1.6 \text{ km s}^{-1}$ , the perturbation wavelength  $\lambda = 2.35 \pm 0.25 \text{ kpc}$ , the pitch angle of the spiral density wave  $i = -5.36^\circ \pm 0.57^\circ$  and the Sun's phase in the spiral density wave  $\chi_\odot = -154^\circ \pm 10^\circ$ . Here, as in the case of solving the model problem (the ‘‘Simulation Results’’ Section), we obtained shifted means of the parameters relative to the solutions obtained at the nominal values of the input data. As a result, we ultimately have the following spiral density wave parameters: the perturbation amplitude  $f_R = 7.7^{+1.7}_{-1.5} \text{ km s}^{-1}$ , the perturbation wavelength  $\lambda = 2.2^{+0.4}_{-0.1} \text{ kpc}$ , the pitch angle of the spiral density wave  $i = -5^{+0.2^\circ}_{-0.9^\circ}$  and the Sun's phase in the spiral density wave  $\chi_\odot = -147^{+3^\circ}_{-17^\circ}$ .

Our values of such parameters as the perturbation amplitude  $f_R$ , the wavelength  $\lambda$ , and the pitch angle of the spiral density wave  $i$  are in good agreement with the results of other authors obtained by analyzing young Galactic disk objects. For example, Mel'nik et al. (2001) found  $f_R = -7 \pm 1 \text{ km s}^{-1}$ ,  $f_\theta = 2 \pm 1 \text{ km s}^{-1}$ , and  $\lambda = 2.0 \pm 0.2 \text{ kpc}$  for  $m = 2$  by analyzing OB associations. Zabolotskikh et al. (2002) found  $f_R = -7 \pm 2 \text{ km s}^{-1}$  and  $f_\theta = -1 \pm 2 \text{ km s}^{-1}$ ,  $i = -6.0 \pm 0.9^\circ$  for  $m = 2$  with a phase  $\chi_\odot \approx -85^\circ$  from the data on young Cepheids ( $P > 9^d$ ) and open star clusters ( $\log T < 7.6$ );  $f_R = -6.6 \pm 2.5 \text{ km s}^{-1}$  and  $f_\theta = 0.4 \pm 2 \text{ km s}^{-1}$ ,  $i = -6.6 \pm 0.9^\circ$  for  $m = 2$  with a phase  $\chi_\odot \approx -97^\circ$  from the data on OB stars. Bobylev and Bajkova (2011) found  $f_R = -12.5 \pm 1.1 \text{ km s}^{-1}$ ,  $f_\theta = 2.0 \pm 1.6 \text{ km s}^{-1}$  (the signs at the amplitudes in the cited papers were reconciled with Eqs. (1) and (2)),  $i = -5.3 \pm 0.3^\circ$  for  $m = 2$  with a phase  $\chi_\odot = -91 \pm 4^\circ$  from the data on OB3 stars with an independent distance scale determined from interstellar Ca II absorption lines.

Nevertheless, we obtained a fairly paradoxical value,  $\chi_{\odot} = -147^{\circ}$ . For young objects, which the masers are, one might expect a phase  $\chi_{\odot} \approx -90^{\circ}$ . Note that analysis of Cepheids yielded  $\chi_{\odot} = -165 \pm 1^{\circ}$  (with the phase measured from the Carina–Sagittarius arm) (Byl and Ovenden 1978),  $\chi_{\odot} = -150^{\circ}$  was found from red supergiants and Cepheids (Mishurov et al. 1979), or  $\chi_{\odot} \approx -290 \pm 16^{\circ}$  (Mishurov et al. 1997) and  $\chi_{\odot} \approx -320 \pm 9^{\circ}$  (Mishurov and Zenina 1999) were found from relatively old Cepheids with periods  $P < 9^d$ . Thus, we get the impression that the masers are intermediate between OB stars and Cepheids in this parameter. The fact that the kinematics of these recently formed stars reflects considerably earlier stages in the motion of regions of active star formation can be a possible explanation. Testing this assumption requires a separate study using reliable data on stellar ages.

## CONCLUSIONS

We proposed a new method of searching for periodicities in the residual velocities of Galactic objects to estimate the parameters describing the Galactic spiral density wave in accordance with the theory of Lin and Shu (1964). In contrast to the method of harmonic analysis of series that we used previously, this method based on a periodogram Fourier analysis takes into account the logarithmic pattern of the Galactic spiral structure and the position angles of Galactic objects. This allows an accurate analysis of the velocities for objects distributed in a wide range of Galactocentric distances to be performed. To increase the significance of the extraction of periodic signals from data series with large gaps, we developed a spectrum reconstruction method based on the generalized maximum entropy method (Bajkova 1992).

Using the proposed methods, we redetermined the Galactic spiral density wave parameters from the radial velocities of 44 masers with known trigonometric parallaxes, proper motions, and line-of-sight velocities. The following spiral density wave parameters were obtained: the perturbation amplitude  $f_R = 7.7_{-1.5}^{+1.7}$  km s<sup>-1</sup>, the perturbation wavelength  $\lambda = 2.2_{-0.1}^{+0.4}$  kpc, the pitch angle of the spiral density wave  $i = -5_{-0.9^{\circ}}^{+0.2^{\circ}}$ , and the phase of the Sun in the spiral density wave  $\chi_{\odot} = -147_{-17^{\circ}}^{+3^{\circ}}$ .

## Acknowledgments

We are grateful to the referees for their useful remarks that contributed to an improvement of the paper. This work was supported by the “Nonstationary Phenomena in Objects of the Universe” Program of the Presidium of the Russian Academy of Sciences and by the “Multiwavelength Astrophysical Research” grant no. NSh–16245.2012.2 from the President of the Russian Federation.

## REFERENCES

1. K. Ando, T. Nagayama, T. Omodaka, et al., Publ. Astron. Soc. Jpn. 63, 45 (2011).
2. Y. Asaki, S. Deguchi, H. Imai, et al., Astrophys. J. 721, 267 (2010).
3. A.T. Bajkova, Astron. Astrophys. Trans. 1, 313 (1992).
4. V.V. Bobylev and A.T. Bajkova, Mon. Not. R. Astron. Soc. 408, 1788 (2010).

5. V.V. Bobylev and A.T. Bajkova, *Astron. Lett.* 37, 526 (2011).
6. V.V. Bobylev, A.T. Bajkova, and A. S. Stepanishchev, *Astron. Lett.* 34, 515 (2008).
7. J. Bovy, D. W. Hogg, and H.-W. Rix, *Astrophys. J.* 704, 1704 (2009).
8. J. Byl and M.W. Ovenden, *Astrophys. J.* 225, 496 (1978).
9. D.P. Clemens, *Astrophys. J.* 295, 422 (1985).
10. S. Dzib, L. Loinard, L.F. Rodriguez, et al., *Astrophys. J.* 733, 71 (2011).
11. B.R. Frieden and A.T. Bajkova, *Appl. Opt.* 33, 219 (1994).
12. C. Goddi, E.M.L. Humphreys, L.J. Greenhill, et al., *Astrophys. J.* 728, 15 (2011).
13. K. Hachisuka, A. Brunthaler, K.M. Menten, et al., *Astrophys. J.* 696, 1981 (2009).
14. T. Hirota, T. Bushimata, Y.K. Choi, et al., *Publ. Astron. Soc. Jpn.* 59, 897 (2007).
15. T. Hirota, T. Bushimata, Y.K. Choi, et al., *Publ. Astron. Soc. Jpn.* 60, 37 (2008a).
16. T. Hirota, K. Ando, T. Bushimata, et al., *Publ. Astron. Soc. Jpn.* 60, 961 (2008b).
17. T. Hirota, M. Honma, H. Imai, et al., *Publ. Astron. Soc. Jpn.* 63, 1 (2011).
18. M. Honma, T. Bushimata, and Y. Choi, *Publ. Astron. Soc. Jpn.* 59, 889 (2007).
19. H. Imai, K. Nakashima, T. Bushimata, et al., *Publ. Astron. Soc. Jpn.* 59, 1107 (2007).
20. E.T. Jaynes, *IEEE Trans. Syst. Sci. Cybern.* 4, 227 (1968).
21. M. K. Kim, T. Hirota, M. Honma, et al., *Publ. Astron. Soc. Jpn.* 60, 991 (2008).
22. C.C. Lin and F.H. Shu, *Astrophys. J.* 140, 646 (1964).
23. P.J. McMillan and J.J. Binney, *Mon. Not. R. Astron. Soc.* 402, 934 (2010).
24. A.M. Mel'nik and A.K. Dambis, *Mon. Not. R. Astron. Soc.* 400, 518 (2009).
25. A.M. Mel'nik, A.K. Dambis, and A.S. Rastorguev, *Astron. Lett.* 27, 521 (2001).
26. K.M. Menten, M.J. Reid, J. Forbrich, et al., *Astron. Astrophys.* 474, 515 (2007).
27. Yu. N. Mishurov and I.A. Zenina, *Astron. Astrophys.* 341, 81 (1999).
28. Yu. N. Mishurov, E.D. Pavlovskaya, and A.A. Suchkov, *Sov. Astron.* 23, 147 (1979).
29. Yu. N. Mishurov, I. A. Zenina, A.K. Dambis, et al., *Astron. Astrophys.* 323, 775 (1997).
30. G.A. Moellenbrock, M.J. Claussen, and W.M. Goss, *Astrophys. J.* 694, 192 (2009).
31. L. Moscadelli, M. J. Reid, K.M. Menten, et al., *Astrophys. J.* 693, 406 (2009).
32. K. Motogi, K. Sorai, A. Habe, et al., *Publ. Astron. Soc. Jpn.* 63, 31 (2011).
33. T. Nagayama, T.Omodaka, A. Nakagawa, et al., *Publ. Astron. Soc. Jpn.* 63, 23 (2011).
34. K. Niinuma, T. Nagayama, T. Hirota, et al., *Publ. Astron. Soc. Jpn.* 63, 9 (2011).
35. C.S. Oh, H. Kobayashi, M. Honma, et al., *Publ. Astron. Soc. Jpn.* 62, 101 (2010).
36. M.J. Reid, K.M. Menten, X.W. Zheng, et al., *Astrophys. J.* 700, 137 (2009).
37. K. Rohlfs, *Lectures on Density Wave Theory* (Springer-Verlag, Berlin, 1977).
38. K.L.J. Rygl, A. Brunthaler, M.J. Reid, et al., *Astron. Astrophys.* 511, A2 (2010).
39. K.L.J. Rygl, A. Brunthaler, A. Sanna, et al., arXiv:1111.7023 (2011).
40. K.M. Sandstrom, J.E.G. Peek, G.C. Bower, et al., *Astrophys. J.* 667, 1161 (2007).
41. A. Sanna, M.J. Reid, T.M. Dame, et al., *Astrophys. J.* 745, 82 (2012).
42. M. Sato, T. Hirota, M.J. Reid, et al., *Publ. Astron. Soc. Jpn.* 62, 287 (2010a).
43. M. Sato, M.J. Reid, and A. Brunthaler, *Astrophys. J.* 720, 1055 (2010b).
44. S. Shiozaki, H. Imai, D. Tafuya, et al., *Publ. Astron. Soc. Jpn.* 63, 1219 (2011).
45. A.S. Stepanishchev and V.V. Bobylev, *Astron. Lett.* 37, 254 (2011).
46. Y.-N. Su, S.-Y. Liu, H.-R. Chen, et al., *Astrophys. J.* 744, L26 (2012).
47. V.V. Vityazev, *Analysis of Nonuniform Time Series* (SPb. Gos. Univ., St.-Petersburg, 2001) [in Russian].
48. Y.Xu, M.J. Reid, X.W. Zheng, et al., *Science* 311, 54 (2006).
49. Y.Xu, L. Moscadelli, M.J. Reid, et al., *Astrophys. J.* 733, 25 (2011).
50. M.V. Zabolotskikh, A.S. Rastorguev, and A.K. Dambis, *Astron. Lett.* 28, 454 (2002).
51. B. Zhang, M.J. Reid, K.M. Menten, et al., *Astrophys. J.* 744, 23 (2012).